一种铁路辙叉用贝氏体钢的焊接热模拟

王秋影[1]， 陈 辉[1]， 胡智博[2]， 江 超[1]， 李 达[1]
(1. 西南交通大学 材料科学与工程学院，成都 610031；2. 铁道科学研究院，北京 100081)

摘 要： 针对一种辙叉用贝氏体钢，采用 Gleeble-3500 对其焊接热循环过程进行了热模拟试验. 采用光学显微镜、扫描电子显微镜、透射电子显微镜和硬度试验对不同冷却速度下焊接热影响区的组织和性能进行研究. 作出加热和冷却膨胀曲线，并采用切线法测定奥氏体转变开始温度(A_{c1})、奥氏体转变结束温度(A_{c3})和不同冷却速度下的相转变温度. 根据试验结果绘出辙叉用贝氏体钢的焊接热影响区连续冷却转变(simulated heat affected zone continuous cooling transforming，SHCCT)曲线，为其焊接性研究提供了基础数据，并用于预测热影响区的组织和性能，可用于指导贝氏体钢辙叉焊接及焊补工艺的优化设计.

关键词： 贝氏体钢；辙叉；SHCCT 图；显微组织；焊接热模拟
中图分类号： TG 401 **文献标识码：** A **文章编号：** 0253－360X(2014)10－0109－04

0 序 言

辙叉是铁路运输的重要组成部件，在铁道结构中是损伤最严重的部位. 贝氏体钢辙叉与高碳钢、高锰钢辙叉相比，在耐磨性、韧性、抗冲击性能等方面具有不可比拟的优势，引起了各国铁路材料研究者们的高度关注，并逐步展开了贝氏体钢力学性能、断裂韧性、CCT 曲线及焊接等相关研究[1,2]. 贝氏体钢要用于铁路线路建设，必然涉及焊接、焊补等关键技术问题，必须首先研究其焊接性. 经过焊接热过程后，热影响区的组织变化及局部硬化会使热影响区的力学性能、耐磨性能等与母材不匹配，焊接材料的加入也会改变接头的组织及性能[3－5]. 热模拟技术是研究焊接热影响区的组织、性能和焊接过程的重要手段[6,7]. 但是，目前国内外关于辙叉用贝氏体钢的热模拟研究很少报道.

文中以一种辙叉用贝氏体钢为研究对象，通过热模拟的方法研究其不同冷却速度下焊接热影响区的组织演变规律，绘出 SHCCT 曲线图，为指导其焊接工艺提供理论依据.

1 试验方法

试验用贝氏体钢的化学成分和基本力学性能测试结果，分别如表 1 和表 2 所示.

焊接热影响区热模拟试验在 Gleeble-3500 热模拟试验机上进行，试样尺寸如图 1 所示. 先以 200 ℃/s 的速度将试样加热至 1 345 ℃，保温 1 s 后，将试样以 40 ℃/s 的冷却速度冷却至 855 ℃. 而后，分别以 0.2，0.5，1，1.5，3，5，7.5，10，15，20，40 ℃/s 一系列不同冷却速度冷却至室温. 在模拟试验过程中，试验机自动记录下热膨胀量随着温度和时间的变化，从而获得膨胀曲线，参照冶金行业标准 YB/T 5127—1993《钢的临界点测定方法(膨胀法)》用切线法测定相转变温度. 贝氏体钢辙叉 SHCCT 曲线

表 1 试验材料成分(质量分数，%)
Table 1 Chemical compositions of experimental material

C	Si	Mn	P	S	Cr
0.292	1.071	1.794	0.012	0.004	1.062
Ni	Mo	Cu	Ti	V	Fe
0.442	0.316	0.152	0.018	0.193	余量

表 2 力学性能测试结果
Table 2 Results of mechanical properties

硬度	抗拉强度	断后伸长率	断面收缩率	冲击吸收功 A_{KV}/J	
H_{HV10}/MPa	R_m/MPa	A(%)	Z(%)	室温	－40 ℃
3 940	1 258	13.2	44.6	21	14

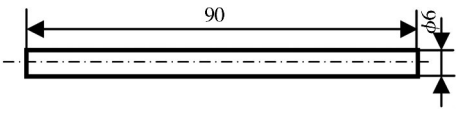

图 1 试样尺寸(mm)
Fig. 1 Specimen size

收稿日期：2014－06－21

测试及绘制，参照冶金行业标准 YB/T 5128—1993《钢的连续冷却转变曲线的测定方法(膨胀法)》.

对热模拟后的试样进行镶嵌、粗磨、抛光，用 3% ~4% 硝酸酒精溶液腐蚀，之后采用 Axio Observer A1m 显微镜和 HITACHI JSM-6490LV 扫描电子显微镜观察其微观组织形貌. 透射试样需先进行粗磨、凹坑，进行离子减薄后采用 Tecnai G2 F20 S-TWIN 透射电子显微镜观察其微观组织形貌. 在试样的选定界面上，采用 HV10 维氏硬度计进行硬度测试，每个试件测试 5 ~7 个点，取平均硬度值.

2 试验结果和讨论

2.1 显微组织分析

不同冷却速度的试样在光学显微镜、扫描电镜及透射电镜下观察到的组织形貌如图 2 和图 3 所示.

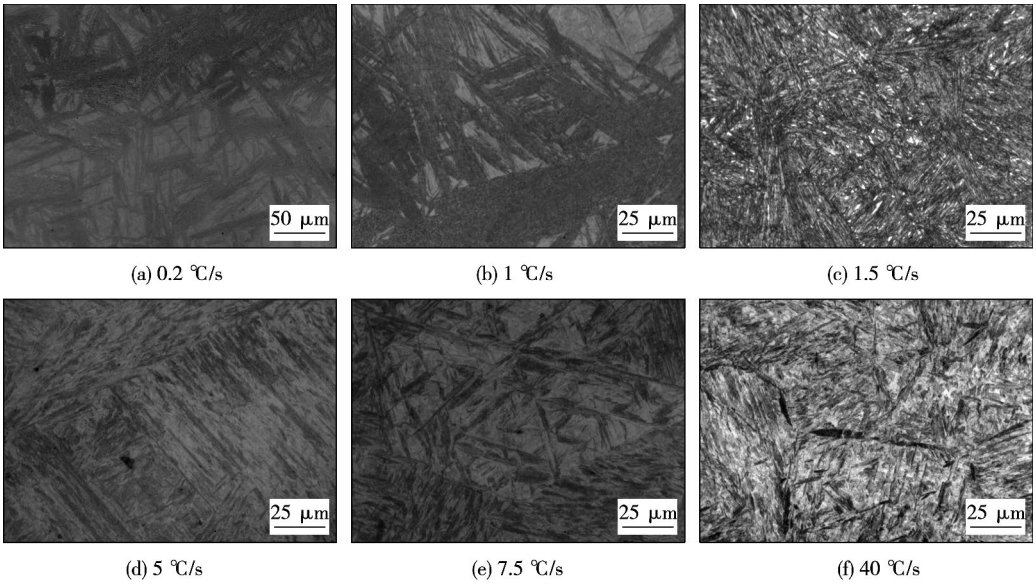

(a) 0.2 ℃/s (b) 1 ℃/s (c) 1.5 ℃/s

(d) 5 ℃/s (e) 7.5 ℃/s (f) 40 ℃/s

图 2 不同冷却速度下试样的组织形貌

Fig. 2 Microstructures at different cooling rates

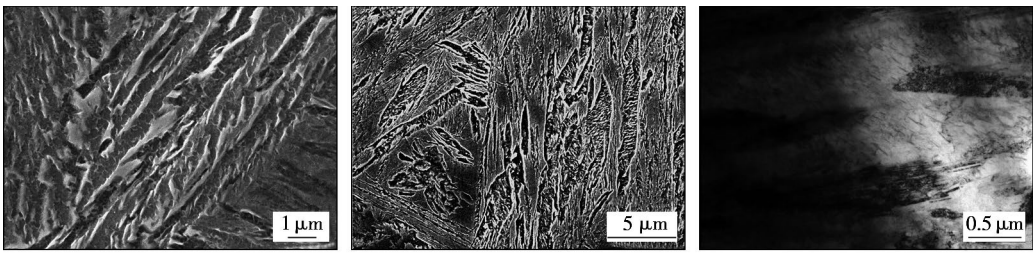

(a) 0.2 ℃/s (b) 3 ℃/s(SEM) (c) 3 ℃/s(TEM)

图 3 扫描电镜和透射电镜形貌

Fig. 3 SEM and TEM images

当冷却速度小于 1 ℃/s 时，在光学显微镜高倍放大后可以看到呈一定角度分布的黑色针状组织(图 2a ~图 2b)[8]. 对 0.2 ℃/s、0.5 ℃/s 冷却速度试样进行显微硬度测试，载荷为 1.96 N，结果如表 3 所示，白色基底的硬度远远高于黑色针状组织. 黑色针状组织为下贝氏体，白色组织为马氏体组织. 由于下贝氏体针是内部碳化物质点有规律、弥散析出成为两相混合物，故易着色，光学显微镜下呈深黑色[8]. 如图 3a 所示，下贝氏体片内的碳化物呈短棒状或纤维状，与主轴的方向交角排列或平行分布[9].

冷却速度为 1.5 ℃/s 时，组织发生明显变化(图 2c). 图 3b 可以看到，冷却速度达 3 ℃/s 时，针片状组织呈岛状分布，且有方向性. 图 3c 可以看到贝氏体马氏体混合组织，其中黑色片状组织为贝氏体. 冷却速度在 1.5 ~5 ℃/s 之间时，显微组织由针状贝氏体、板条状贝氏体和马氏体组成，如图 2c ~图 2d 和图 3b ~图 3c 所示.

表 3　显微硬度测试结果

Table 3　Results of microhardness test

冷却速度 v/(℃·s^{-1})	组织形态	维氏硬度 $H_{HV0.2}$/MPa					
		1	2	3	4	5	平均值
0.2	黑色针状	3 528	3 146	3 842	3 812	3 450	3 557
	白色基底	4 077	4 400	4 684	4 557	4 371	4 420
0.5	黑色针状	4 939	4 430	3 606	4 077	3 900	4 194
	白色基底	5 772	6 223	4 763	5 635	6 772	5 831

如图 2e 所示,冷却速度为 7.5 ℃/s 时,发现“△”状组织,为板条马氏体的典型形貌[10]. 冷却速度增大至 10 ~ 40 ℃/s 时,也均有典型板条马氏体特征,此时组织以板条马氏体组织为主(图 2f). 7.5 ℃/s 可以视为获得马氏体组织的临界冷却速度,低于 7.5 ℃/s 时可得到贝氏体和马氏体的混合组织,高于 7.5 ℃/s 时得到以马氏体为主的组织.

2.2　硬度分析

硬度测试结果如表 4 和图 4 所示. 通过非线性拟合,得到冷却速度与硬度之间的定量关系表达式[15]为

$$H_{HV} = 5\,927.6 - 1\,227.7e^{-v/0.9} - 545.4e^{-v/13.4} \quad (2)$$

式中: H_{HV}为维氏硬度; v 为冷却速度.

可以看出,热模拟试样的硬度均高于母材,硬度随着冷却速度的增大而增大. 当冷却速度小于 1 ℃/s时,随着冷却速度的增大,针状贝氏体的数量减少,马氏体数量增多,硬度由 460 MPa 增大到 509 MPa. 冷却速度在 1.5 ~ 5 ℃/s 之间时,显微组织均为贝氏体和马氏体混合组织,硬度变化不大. 当冷却速度大于 7.5 ℃/s 时,显微组织变为以板条马氏体为主,硬度也相应地增大到 579 ~ 600 MPa 之间,冷却速度对硬度的影响不大.

2.3　相变点的确定

用切线法测得奥氏体转变开始温度(A_{c_1})、奥氏体转变结束温度(A_{c_3})和马氏体转变开始温度(M_s)分别为 745,882 和 386 ℃,如图 5,图 6 所示. 用同样的方法测得不同冷却速度下的相转变温度如表 4 所示.

表 4　不同冷却速度下硬度和相转变温度

Table 4　Hardnesses and phase transition temperatures at different cooling rates

冷却速度 v/(℃·s^{-1})	维氏硬度 H_{HV10}/MPa	相转变温度 T_p/℃	冷却速度 v/(℃·s^{-1})	维氏硬度 H_{HV10}/MPa	相转变温度 T_p/℃	冷却速度 v/(℃·s^{-1})	维氏硬度 H_{HV10}/MPa	相转变温度 T_p/℃
0.2	460	452	3.0	560	427	15	580	356
0.5	462	439	5.0	550	384	20	600	388
1.0	509	465	7.5	579	386	40	600	395
1.5	547	410	10	581	368			

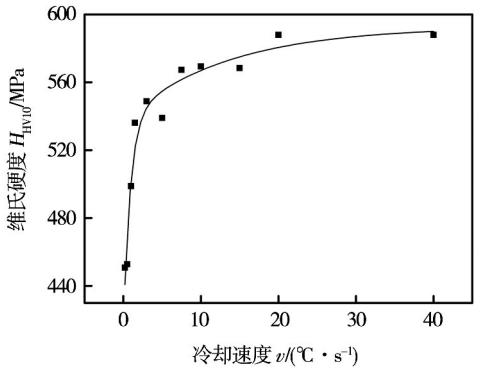

图 4　硬度变化曲线

Fig. 4　Hardness curve

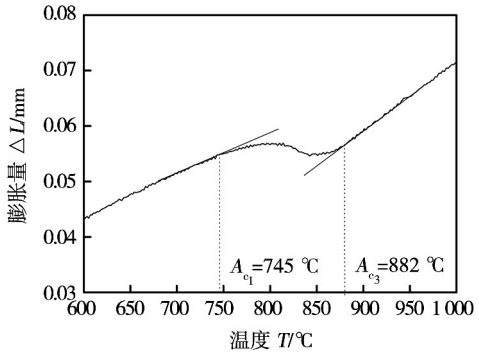

图 5　0.2 ℃/s 加热膨胀曲线

Fig. 5　0.2 ℃/s heating expanding curve

2.4　SHCCT 图分析

根据采集到的数据,绘出温度—时间(对数)的坐标中不同冷却速度下的冷却曲线,并进行拟合使曲线更加光滑美观. 然后,将不同冷却速度下的相转变点用光滑曲线描述在温度—时间(对数)的坐标中. 最后,将不同冷却速度下的组织组成标在相应位置. 得到贝氏体钢的 SHCCT 曲线,如图 7 所示.

由图 7 可以看出,SHCCT 曲线中只有贝氏体转变区和马氏体转变区. SHCCT 曲线在焊接过程中起着非常重要的作用,不仅可以用于预测 HAZ 的组织

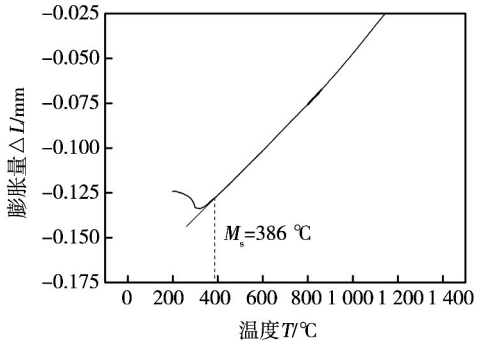

图 6 7.5 ℃/s 冷却膨胀曲线

Fig. 6 7.5 ℃/s cooling expanding curve

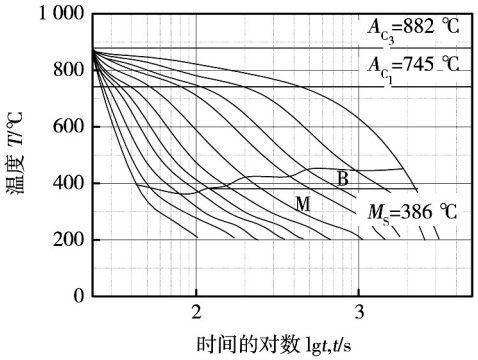

图 7 SHCCT 曲线

Fig. 7 SHCCT diagram

和性能，还可以用于指导实际焊接工艺，贝氏体钢的 SHCCT **曲线对贝氏体钢辙叉的焊接工艺及焊补修复工艺，有着十分重要的指导意义.**

3 结 论

(1) 当冷却速度小于 1 ℃/s **时，试样的显微组织为针状下贝氏体和马氏体混合组织. 冷却速度为** 1.5 ~ 5 ℃/s **之间时，出现板条状贝氏体组织，且马氏体随着冷却速度的增大而增多. 冷却速度大于** 7.5 ℃/s **时，组织均以马氏体为主.**

(2) 冷却速度小于 5℃/s **时，随着冷却速度的增大硬度显著增大. 硬度和冷却速度之间有定量关系式:** $H_{HV} = 5\ 927.6 - 1\ 227.7e^{-\nu/0.9} - 545.4e^{-\nu/13.4}$.

(3) 试验用贝氏体钢的 SHCCT **图中只有贝氏体和马氏体转变区. 当冷却速度低于** 7.5 ℃/s **时，存在贝氏体和马氏体转变; 冷却速度高于** 7.5 ℃/s **时，只有马氏体转变.**

参考文献:

[1] **魏秋明，周鹿宾.** Si-Mn-Mo **系低碳贝氏体钢焊接热影响区过热带的组织分析** [J]. **焊接学报，**1989，10(1)：30 - 35.
Wei Qiuming，Zhou Lubin. Microstructures of simulated HAZ of low carbon Si-Mn-Mo bainitic [J]. Transactions of the China Welding Institution，1989，10(1)：30 - 35.

[2] **李 璟，商存亮，王立群，等. 低碳贝氏体钢连续冷却相变规律研究** [J]. **河南冶金，**2011，19(3)：15 - 17.
Li Jing，Shang Cunliang，Wang Liqun，*et al*. Research on phase transformation pattern under continuous cooling for low carbon bainitic steel [J]. Henan Metallurgy，2011，19(3)：15 - 17.

[3] Qian L H，Zhou Q，Zhang F C，*et al*. Microstructure and mechanical properties of a low carbon carbide-free bainitic steel co-alloyed with Al and Si [J]. Materials and Design，2012，39：264 - 268.

[4] **王 鑫. 贝氏体钢辙叉与** U71Mn **钢钢轨的焊接** [D]. **秦皇岛：燕山大学，**2008.

[5] Parzych S，Krawczyk J. The influence of heat treatment on microstructure and tribological properties of resistance butt welds made of a cast bainitic steel [J]. Archives of Metallurgy and Materials，2012，57：261 - 264.

[6] **谭佃龙，章三红，贺信莱，等. 超低碳贝氏体钢焊接热影响区研究** [J]. **焊接学报，**1996，17(3)：139 - 144.
Tan Dianlong，Zhang Sanhong，He Xinlai，*et al*. A study on HAZ of ultra-low carbon bainitic steel [J]. Transactions of the China Welding Institution，1996，17(3)：139 - 144.

[7] **王旭友，腾 彬，雷 振，等.** JFE980S **高强钢激光 - 电弧复合热源热模拟试验分析** [J]. **焊接学报，**2010，31(11)：25 - 28.
Wang Xuyou，Teng Bin，Lei Zhen，*et al*. Analysis on laser-arc hybrid welded joint of high strength steel JFE980S by thermal simulation test [J]. Transactions of the China Welding Institution，2010，31(11)：25 - 28.

[8] **苏德达，郭建国，胡建文，等. 板条马氏体和下贝氏体转变过程的动态观察** [C] // **中国机械工程学会热处理分会，太原理工大学. 国际材料科学与工程学术研讨会论文集(下册). 天津：天津大学出版社，**2005：743 - 753.

[9] **徐学利，辛希贤，石 凯，等. 焊接热循环对** X80 **管线钢粗晶区韧性和组织性能的影响** [J]. **焊接学报，**2005，26(8)：69 - 72.
Xu Xueli，Xin Xixian，Shi Kai，*et al*. Influence of welding thermal cycle on toughness and microstructure in grain-coarsening region of X80 pipeline steel [J]. Transactions of the China Welding Institution，2005，26(8)：69 - 72.

[10] **张明星，康沫狂. 低、中碳合金钢中的马氏体与贝氏体形态** [J]. **钢铁研究学报，**1993，5(4)：59 - 63.
Zhang Mingxing，Kang Mokuang. Morphology of martensite and bainite in low and medium carbon alloy steels [J]. Journal of Iron and Steel Research，1993，5(4)：59 - 63.

作者简介: 王秋影，女，1990 **年出生，博士研究生. 主要从事高速铁路焊接技术、激光 - 电弧复合焊接相关的研究工作. 发表论文** 5 **篇.** Email: wangqiuying@my.swjtu.edu.cn

通讯作者: 陈 辉，男，教授，博士研究生导师. Email: xnrpt@163.com

of Mechanical & Electronic Engineering, China University of Petroleum, Qingdao 266555, China). pp 93 – 96

Abstract: Based on SYSWELD software, a method verified the parameters of heat source and heat input of double ellipsoid mode and two principles guiding how to determine the above parameters were put forward. Through taking the above mentioned measures, the trailing problem of molten pool rear in Guassian and double ellipsoid mode had been successfully solved. The experimental results show that the predicted shape and trend fusion line on top surface and cross section are in agreement with the experimental measurements. It provides theoretical basis and basic data for precise modeling and intelligent control of TIG welding process. The reason why so marked difference between the predicted and practical trend fusion line at the rear of the pool exists was analyzed, which could provide a guide for the future research.

Key words: double ellipsoid heat source; molten pool geometry; finite element method; gas tungsten arc welding; rear trailing of molten pool

Quantitative analysis of solder powder particle based on morphology LU Lin[1,2], SUN Jia[1], WANG Hongmei[1], WANG Liqiang[3] (1. School of Chemical Equipment, Shenyang University of Technology, Shenyang 111003, China; 2. State Key Laboratory of Advanced Welding and Joining, Harbin Institute of Technology, Harbin 150001, China; 3. University of Dayton, Dayton 45469, America). pp 97 – 100

Abstract: Description and statistical analysis to solder powder particle shape, which is made by ultrasonic atomization, have performed by using morphological methods since high angularity of solder powder particle and less regular shape which are key factors affecting the quality of solder paste preparation. Two important characteristics of solder powder particle shape, solder powder particle fractal dimension and aspect ratio, have been established. Firstly, the geometric projection image of solder powder particle was calculated, and then corrosion and expansion methods of morphology to characterize solder powder particle profiles were done. Moreover, the pattern information on the particle number and radius were statistically calculated. Finally fitting equation with fractal dimension was built. The experimental results showed that the morphological methods submitted by this article can be applied to segmentation adhesion welding particle image. In addition, the aspect ratio and fractal dimension of solder powder particle accurately reflect the solder powder particle real shape.

Key words: lead-free solder powder particles; fractal dimension; image processing; corrosion transformation; dilatation transformation

Analysis on welding porosity of iron powder electrode YIN Shike[1], WU Shuxiong[2], WANG Yong[1], WANG Yishan[1] (1. China Iron and Steel Research Institute Group, Beijing 100081, China; 2. Beijing Miller Electric MFG. Co. Ltd., Beijing 100023, China). pp 101 – 104

Abstract: To determine the nature of the porosity, the gas compositions in porosity were tested by suspension melting-gas chromatography apparatus. The photograph of internal porosity was also observed by SEM. The analysis result shows that the gas compositions of porosity are the same mixed ones of CO and H_2 in both basic and acid electrodes. CO may be considered to play an important role in the formation of porosity. Two kinds of shapes are shown in the interior porosity. The one is worm-like porosity which situated in the middle and upper weld metal, and the other is conchoidal porosity which can be found at the root pass. The analysis result also shows that, whether the formation of porosity or nat, can be predicted by the diffusible hydrogen content of weld metal.

Key words: powder electrode; arc welding; interior porosity; diffusible hydrogen content

Weldability of Al-13.0Si-0.7Mg Alloy on T6 state TENG Yingxue[1], ZHANG Yuqi[2], GUO Jing[1], YANG Chunli[2] (1. School of Materials and Metallurgy, University of Science and Technology LiaoNing, Anshan 114001, China; 2. State Key Laboratory of Advanced Welding and Joining, Harbin Institute of Technology, Harbin 150001, China). pp 105 – 108

Abstract: Experiment of flat butt-welding is conducted on the Al-13.0Si-0.7Mg alloy on T6 state with two kinds of welding wire, ER4047 and ER5183. The process of double pulse MIG welding by both sides is used to reduce the influence of welding heat input on the base metal. The welding parameters of two welding wires are confirmed and the good weld formations are obtained. The alloy and the two wires to this alloy have good heat cracking resistance as fish-bone cracking test shows. On this basis, the microstructure observation and mechanics performance testing are conducted on the welding joints. The results show that the microstructure of joints is different for these two wires. The tensile strength of the welded joints is about 70% of the one of base metal. The hardness test indicates that there is softening phenomenon in the heat-affected zone.

Key words: Al-13.0Si-0.7Mg alloy; fish-bone cracking test; microstructure; mechanical properties

Welding thermal simulation of bainite steel used for rail way frog WANG Qiuying[1], CHEN Hui[1], HU Zhibo[2], JIANG Chao[1], LI Da[1] (1. School of Material Science and Engineering, Southwest Jiaotong University, Chengdu 610031, China; 2. China Academy of Railway Science, Beijing 100081, China). pp 109 – 112

Abstract: Gleeble-3500 was used to simulate the thermal cycle processes of bainite steel used for frog. The microstructure and properties of HAZ were investigated by optical microscopy (OM), scanning electron microscopy (SEM), transmission electron microscopy (TEM) and hardness test, respectively. The start temperature of austenite transformation, the end temperature of austenite transformation and the phase transition temperatures under different cooling rates were measured by the tangent method from the expanding curves. According to the experimental results, the simulated heat affected zone continuous cooling transforming (SHCCT) diagram of the bainite steel was constructed. SHCCT diagram provides basic data for the research of its weldability. It could be used to predict microstructure and properties of HAZ and optimize welding and repair welding processes of bainite steel frog.

Key words: bainite steel; frog; SHCCT diagram; microstructure; welding thermal simulation